International Journal of Multiphase Flow 69 (2015) 54–62

Contents lists available at ScienceDirect

International Journal of Multiphase Flow

journal homepage: www.elsevier.com/locate/ijmulflow

Modulated flow pattern in a condenser tube with two-phase flow interacting with mesh screen surface at micro-gravity

Dongliang Sun [a,b], Jinling Xu [b,*], Qicheng Chen [b], Yuying Yan [c,*]

[a] School of Mechanical Engineering, Beijing Institute of Petrochemical Technology, Beijing 102617, China
[b] Beijing Key Laboratory of Multiphase Flow and Heat Transfer, North China Electric Power University, Beijing, China
[c] Energy & Sustainability Research Division, Faculty of Engineering, University of Nottingham, UK

ARTICLE INFO

Article history:
Received 15 June 2014
Received in revised form 8 October 2014
Accepted 4 November 2014
Available online 13 November 2014

Keywords:
Phase separation condenser tube
Mesh cylinder
Flow pattern modulation
Condensation heat transfer

ABSTRACT

Two-phase loop systems are important to maintain low temperature in a spacecraft at micro-gravity. It is known that the condenser size at micro-gravity can be one order magnitude larger than that at the earth gravity. This paper explores the effectiveness of the modulated flow technique at micro-gravity for the condensation heat transfer enhancement. A mesh cylinder is suspended in a tube, dividing the tube cross section into annular region and core region. When an intermittent two-phase flow interacts with the mesh screen structure, gas bubbles are prevented from entering the mesh cylinder thus they flow in the annular region to form the thin liquid film on the wall. Liquid can be separated to flow in the core region. Here the bubble dynamics in the bare tube section and modulated flow section are investigated for three different slug flow cases. It is found that the mesh cylinder modulates the slug flows in the bare tube section to form the elongated-ring-slug bubble train in the modulated flow section. Liquid plugs can disappear due to the continuous liquid flow from the annular region to the core region. Thus the two-phases are thoroughly separated with gas flowing in the annular region, forming ultra-thin liquid film thicknesses on the wall at micro-gravity. The modulated flow pattern forms the liquid film thicknesses to be about 1/30–1/10 of those in the bare tube section for the three cases. Based on the modulated bubble dynamics and parameters, the condensation rates per unit wall area ($\dot{m}$) can be about 10–100 times of those in the bare tube section for the three cases. The modulated flow pattern and enhanced heat transfer are more obvious when the gas volume flow rates are decreased. This study provides a new approach to enhance the condensation heat transfer for space applications under micro-gravity environment.

Introduction

Due to the requirements of decreased weight and compact size for large spacecraft such as the International Space Station, two-phase loop systems (Delil et al., 2002; Haobo and Reinhard, 2002; Kaya et al., 2008) have been developed to maintain low temperatures within the spacecraft depot. Two-phase loop systems have the advantages of large heat transfer capability, uniform temperature distribution and small pumping power, etc., thus they are more attractive for space applications. The two-phase loop systems involve an evaporation process to extract heat from the spacecraft depot and a condensation process to reject the heat to the outer environment.

Condensers are usually too large to meet the size and weight constraints at the normal gravity (Kim and Mudawar, 2012). It is known that the condensation heat transfer coefficients are lower at micro-gravity. Condensation at micro-gravity is a challenging issue. Fig. 1 shows the liquid film distribution over the tube cross section at the earth gravity (horizontal flow) and at the micro-gravity. Micro-gravity omits the buoyancy force between liquid and gas phases, thus liquid films are uniformly distributed on the wall and they are thick to worsen the condensation heat transfer. Da Riva and Sanz (1991) numerically investigated the condensation heat transfer in horizontal tubes with different working fluids. They found that the condenser tube lengths at micro-gravity are 28, 19, 15 and 18 times of those at the earth gravity for vapors of ammonia, water, R1 and R22, respectively (see Fig. 1). Delil (1998) computed the ammonia vapor condensation heat transfer in a 16.1 mm diameter tube at the earth gravity and micro-gravity. The flow direction was downward. It was found that the condenser tube length at micro-gravity is eleven times of that at the earth

* Corresponding authors. Tel./fax: +86 10 61772268 (J. Xu). Tel./fax: +44 0115 951 3168 (Y. Yan).
E-mail addresses: xjl@ncepu.edu.cn (J. Xu), yuying.yan@nottingham.ac.uk (Y. Yan).

http://dx.doi.org/10.1016/j.ijmultiphaseflow.2014.11.001
0301-9322/

gravity. In summary, the tube length required to achieve complete condensation at the micro gravity is an order of magnitude larger than that at the normal gravity. New approach to make compact condensation tube at the micro-gravity is necessary.

Conventionally, microstructures on the tube wall enhance the condensation heat transfer. The micro groove tubes (Graham et al., 1998), micro-fin tubes (Cavallini et al., 2000), herringbone tubes (Miyara and Otsubo, 2002) and helically corrugated tubes (Suriyan and Somchai, 2010) belong to the enhanced condensation tubes. The heat transfer enhancement mechanism is attributed by mixing the fluid boundary layers and limiting the growth of fluid boundary layers close to the wall surfaces.

Recently, a phase separation condenser tube was proposed by our group to modulate flow patterns for enhancing condensation heat transfer at the normal gravity environment (Chen et al., 2012, 2013; Sun et al., 2013). A mesh cylinder is suspended in a tube, dividing the tube cross section into an annular region and a core region. When an intermittent two-phase flow interacts with the mesh screen structure, gas bubbles are prevented from entering the mesh cylinder inside due to the surface tension effect, if the mesh pores are small enough. This ensures the gas phase flowing in the annular region close to the wall, creating thin liquid films on the wall to enhance the condensation heat transfer. The pressure driven flow pushes liquids towards the core region of the tube and liquids flow there. The phase separation condenser tube is called due to the separated flow paths of gas and liquid phases in two different regions. The objective of this study is to explore the possibility that the phase separation condenser tube can be used at the micro-gravity environment. We investigate how the negligible buoyancy force between two-phases affects the modulated flow structure at micro-gravity. In order to do so, the forced convective adiabatic air–water slug flow is analyzed. The modulated flow pattern and related dynamic and stable parameters are discussed at the micro-gravity.

The physical structure

The phase separation condenser tube

Fig. 2a shows the phase separation condenser tube. Fig. 2b shows the metallic mesh screen structure, suspending in the tube. The mesh cylinder includes a flat bottom mesh pore surface and a circular side mesh pore surface. The mesh cylinder exit is open to discharge the separated liquid. The mesh cylinder inside is empty. The new condenser tube consists of a bare tube section 1 and a modulated flow section. In the modulated flow section, the tube cross section is divided into an annular region 3 and a core region 2, interfaced by the mesh pore surface. Table 1 shows the geometric parameters for the condenser tube.

During the condensation process, the flow evolves several flow patterns as annular flow and intermittent (slug, plug and bubble) flow consecutively along the flow direction. The annular flow maintains higher heat transfer coefficients in the tube upstream due to the thin liquid film. However, the thick liquid film thickness for the intermittent (slug, plug and bubble) flow deteriorates the heat transfer, yielding the decreased heat transfer coefficients along the flow length. The modulated flow section tackles the thick liquid film issue for intermittent flow patterns, thus it is arranged from a specific distance away from the tube inlet. In this study, the bare tube section arrangement is to compare the bubble dynamics between the modulated flow section and bare tube section.

The 3D to 2D-axisymmetric conversion of mesh screen

Fig. 2b shows a practical 3D mesh screen used in our experiment. The square mesh wire has a thickness of $\delta = 70$ μm. The square mesh pore has a width of $w = 150$ μm. The number of mesh pores attains about 240,000 for a mesh cylinder with its diameter of 10.36 mm and length of 350 mm. The grid number required is in the order of 100-million, making impossible to fulfill the numerical simulation. It is necessary to perform the 3D to 2D-axisymmetric conversion for simplification purpose.

The 3D mesh screen can be converted into a 2D-axisymmetric stripe-type mesh screen, by replacing δ and w (see Fig. 2b) with the stripe-type mesh wire thickness of δ' and stripe-type mesh pore gap of w' (see Fig. 2c). The following criteria should be satisfied:

The equal equivalent diameter criterion: the square mesh pore has an equivalent diameter of w, and the stripe-type mesh pore has an equivalent diameter of $2w'$. The equal equivalent diameter criterion for both types of mesh pores yields $w' = 0.5w$.

The equal flow area criterion: the projective area of the total mesh pores (see Fig. 2b) should be equal to that shown in Fig. 2c. The equal flow area criterion gives $[w/(w+\delta)]^2 = w'/(w'+\delta'')$. Thus we have $\delta' = \delta + \delta^2/2w$.

The equal capillary pressure criterion: the capillary pressure influences the gas–liquid interface near mesh pores. Once the above equal equivalent diameter and flow area criteria are satisfied, the equal capillary pressure criterion is automatically satisfied. This is because the capillary pressure created by the square mesh pores is $\Delta p = 4\sigma\cos\theta/w$, which equals to $\Delta p = 2\sigma\cos\theta/w'$ for the stripe-type mesh pores, where σ is the surface tension coefficient and θ is the contact angle.

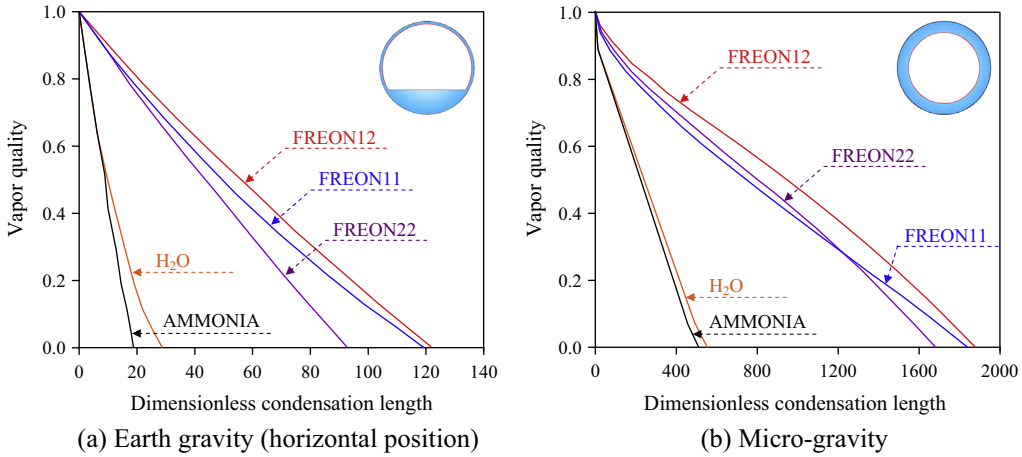

Fig. 1. Vapor quantity versus diemensionless condensation length (Da Riva and Sanz, 1991).

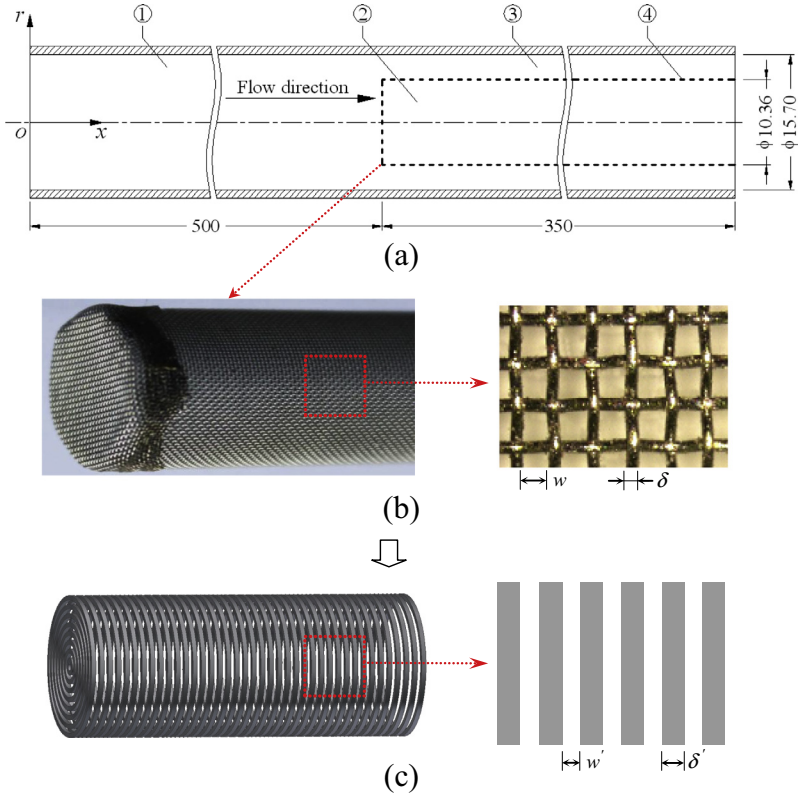

Fig. 2. The phase separation condenser tube and the 3-D to 2-D conversion of mesh cylinder (unit: mm). (a) The tube configuration, 1. bare tube section, 2. core region, 3. annular region, 4. mesh cylinder; (b) practical 3D mesh cylinder; (c) transformed 2D-axisymmetric stripe-type mesh cylinder.

Table 1
Structure parameters of the phase separation condenser tube.

L_b	Bare tube section length (500.0 mm)	L_m	Modulated flow section length (350.0 mm)
D	Bare tube diameter (15.7 mm)	D_m	Mesh cylinder diameter (10.36 mm)
δ	Square mesh wire thickness (70 μm)	w	Square mesh pore width (150 μm)
δ'	Stripe-type mesh wire thickness (86 μm)	w'	Gap of stripe-type mesh pore (75 μm)

The above deduction yields $w' = w/2 = 75$ μm and $\delta' = \delta + \delta^2/(2w) = 86$ μm. After the conversion, the number of stripe-type mesh pores is reduced to about 2200 for a 350 mm long mesh cylinder.

The numerical model and solution method

We investigate the forced convective adiabatic air–water slug flows in both the bare tube section and modulated flow section at the micro-gravity ($g = 0$ m/s^2). Three air–water slug flow cases are computed (see Table 2), in which u_{in} is the inlet velocity, J is the superficial velocity, Re is the Reynolds number, and the subscripts l and g denote the liquid and gas phases, respectively. The two-phase superficial velocities are defined as

$$J_l = \frac{u_{in,l}(R^2 - R_{in,g}^2)}{R^2}, \quad J_g = \frac{u_{in,g}R_{in,g}^2}{R^2} \tag{1}$$

Table 2
Operating conditions for three different air–water slug flows.

Case	$u_{in,l}$ (m/s)	$u_{in,g}$ (m/s)	J_l (m/s)	J_g (m/s)	Re_l	Re_g
Case 1	0.1023	0.1046	0.066	0.037	1031.2	39.8
Case 2	0.1023	0.0523	0.066	0.0185	1031.2	19.9
Case 3	0.1023	0.02615	0.066	0.00925	1031.2	9.95

where the bare tube radius of R is 7.85 mm and the gas inlet radius of $R_{in,g}$ is 5.2 mm (see Fig. 3). The two-phase Reynolds numbers are defined in terms of the superficial velocities:

$$Re_l = \frac{2RJ_l\rho_l}{\mu_l}, \quad Re_g = \frac{2RJ_g\rho_g}{\mu_g} \tag{2}$$

where ρ is density and μ is dynamic viscosity. Because the two-phase Reynolds numbers for the three cases are all less than 2000, the slug flows are incompressible, laminar and unsteady two-phase flow problems. Fig. 3 shows the two-dimensional axial-symmetric coordinate (r–x) system. The original point is at the tube center in the tube entrance.

Governing equations

The main numerical methods for two-phase flows include the particle-trajectory model (Salewski and Fuchs, 2007), two-fluid model (Morales-Ruiz et al., 2012), and volume of fluid (VOF) method (Hirt and Nichols, 1981), etc. Zu and Yan (2009) and Zu et al. (2011) have shown that the VOF method can capture the interface and calculate the surface tension force accurately. Therefore, this study applies the VOF method embedded in FLUENT software to perform the numerical simulations. The volume fraction α, whose value lies between 0 and 1, is defined in the VOF method.

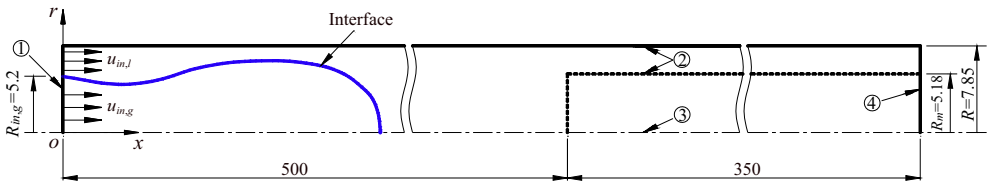

Fig. 3. The computation region and boundary conditions (unit: mm), 1. velocity-inlet boundary condition, 2. wall boundary condition, 3. axial symmetric boundary condition, 4. pressure-outlet boundary condition.

For gas–liquid two-phase flow problems, the sum of the gas and liquid volume fractions equals to unity in each grid.

$$\alpha_g + \alpha_l = 1 \tag{3}$$

The whole computation domain only needs one set of governing equations when the VOF method is used. The advection equation of the gas volume fraction is

$$\frac{\partial \alpha_g}{\partial t} + \nabla \cdot (\vec{v}\,\alpha_g) = 0 \tag{4}$$

where t is the time and $\vec{v}$ is the velocity vector

The continuity equation is

$$\nabla \cdot \vec{v} = 0 \tag{5}$$

The momentum equation is

$$\frac{\partial}{\partial t}(\rho \vec{v}) + \nabla \cdot (\rho \vec{v}\,\vec{v}) = -\nabla p + \nabla \cdot [\mu(\nabla \vec{v} + \nabla \vec{v}^T)] + \vec{F}_{vol} \tag{6}$$

where p is the pressure, $\vec{F}_{vol}$ is the surface tension force. The density and viscosity are calculated by the following equations:

$$\rho = \rho_l \alpha_l + \rho_g \alpha_g \tag{7}$$

$$\mu = \mu_g \alpha_g + \mu_g \alpha_g \tag{8}$$

The surface tension force is calculated based on the CSF (Continuum Surface Force) model (Brackbill et al., 1992):

$$\vec{F}_{vol} = \sigma \frac{\alpha_l \rho_l \kappa_l \nabla \alpha_l + \alpha_g \rho_g \kappa_g \nabla \alpha_g}{0.5(\rho_l + \rho_g)} \tag{9}$$

where σ is the surface tension coefficient, κ is the interface curvature having the following expression:

$$\kappa_l = -\kappa_g = -\nabla \cdot \left(\frac{\nabla \alpha_l}{|\nabla \alpha_l|} \right) \tag{10}$$

Boundary conditions

Fig. 3 shows the computation domain and corresponding boundary conditions used in this study. The inlet condition for both gas and liquid phases can be written as

$$u = \begin{cases} u_{in,g} & 0 < r < R_{in,g} \\ u_{in,l} & R_{in,g} \le r < R \end{cases}, \quad v = 0 \tag{11}$$

$$\alpha_g = \begin{cases} 1 & 0 < r < R_{in,g} \\ 0 & R_{in,g} \le r < R \end{cases}, \quad \alpha_l = \begin{cases} 0 & 0 < r < R_{in,g} \\ 1 & R_{in,g} \le r < R \end{cases} \tag{12}$$

where R is the bare tube radius, $R_{in,g}$ is the gas inlet radius, u and v are axial and radial velocities respectively.

The no-slip boundary conditions were applied on the tube wall and mesh wire surface, i.e. $u = v = 0$. The contact angle shall be introduced when gas phase directly contacts with the solid wall, or when the liquid film thickness is smaller than the distance that the van der Waal forces can act across the film. In this study, there is indeed a liquid film beneath the gas bubble on the solid wall. The minimum liquid film thickness is larger than 30 μm, which is significantly larger than the distance that the van der Waal forces can act on the film. Thus the contact angle effect is neglected. Such treatment is similar to that in Mehdizadeh et al. (2011).

The boundary condition along symmetric axis can be expressed as $\partial\phi/\partial r = 0$ where ϕ can be u or α, $v = 0$. The boundary condition at exit of the computation domain is pressure-outlet boundary condition.

Grid system

Due to the inserted mesh cylinder, there are three types of geometric scales: macro scale of bare tube section and core region, miniature scale of annular region, and micron scale of mesh pores. For such a complicated multiscale geometric structure, the grid number will be significantly large if one uses the uniform grid system. Here we adopt different grid sizes to different geometry scales. The average grid sizes are 375 μm in the bare tube section and core region, 100 μm in the annular region, and 18.75 μm near the mesh pores. The different grid sizes are linked with each other by adapting the transition factor of 5:1. The grid size along the radial direction is 10 μm for the first layer of the tube wall. Fig. 4 illustrates the multiscale grid system for the phase separation condenser tube. In order to accurately capture the bubble interface, a dynamic grid adaption method is used near the bubble interface, with two level of grid refinement. The grids are refined by sixteen times near the bubble interface. Further grid refinement yields no significant improvement of the computation results.

Solution method

The governing equations are discretized by the finite-volume method (FVM) (Patankar, 1980; Tao, 2001). The second order upwind scheme is adopted for the convection term in the momentum equation (Eq. (6)). The advection equation of volume fraction (Eq. (4)) is solved by the geometric reconstruction scheme (PLIC). The continuum and momentum equations (Eqs. (5) and (6)) are coupled by the SIMPLE method. The first-order implicit scheme treats the time marching of the continuity and momentum equations. The time step Δt is controlled by a specified maximum value for the Courant number, which is defined as

$$Co = \frac{\Delta t}{\Delta x / |\vec{v}|} \tag{13}$$

where Δx is the grid size and $|\vec{v}|$ is the fluid velocity within the grid. We set a maximum Courant number of 0.25 and use a variable time step based on the Courant number.

Results and discussion

Verification

The experiment data at the earth gravity (laboratory environment) are used to verify the numerical model and solution method.

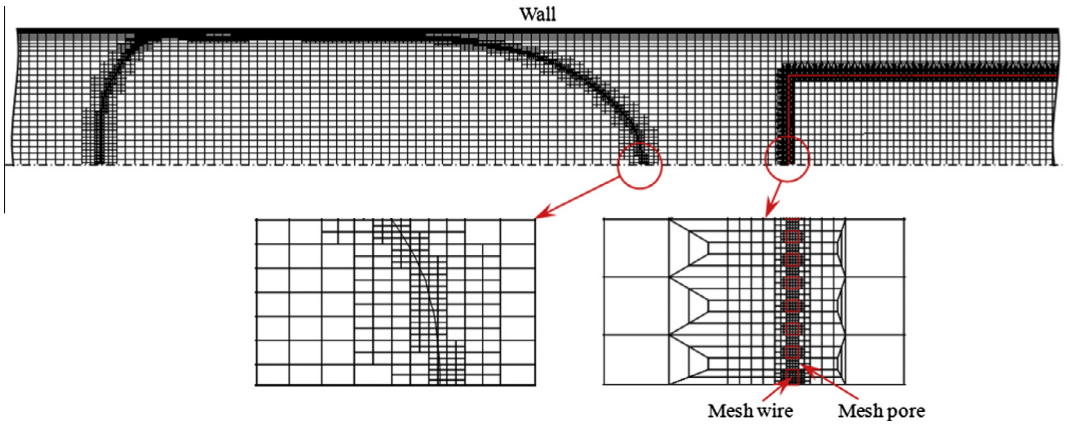

Fig. 4. The multiscale grid system for the phase separation condenser tube.

The structure adopted for verification is exactly identical to that used for this numerical simulation (see Fig. 2). The flow direction is upward with the gravity force ($g = 9.81$ m/s^2) against the bulk flow direction. The running parameters used for verification is the same as Case 1 (see Table 2). Fig. 5 shows the measurement and numerical results at the normal gravity. The measured bubble shapes, lengths and velocities agree very well with the numerical results in both the bare tube section and modulated flow section. Fig. 5 gives the strong evidence that the numerical model and solution method is accurate and feasible.

Flow pattern modulation process

Fig. 6 shows the bubble shape and flow field in the bare tube section (Fig. 6a and b), across the mesh cylinder region (Fig. 6c), and in the modulated flow section (Fig. 6d and e) for Case 1 at $t = 7.933$ s. Here t is the time, x_s and x_e are the starting and ending coordinates of the focused area, respectively.

Fig. 6a illustrates the bubble pattern in the tube entrance. After the bubble formed, the bubble becomes bullet-like and then moves forward without any shape change in the bare tube section. Because the micro-gravity yields no buoyancy force on the bubble, there are no vortexes in liquid plugs (see Fig. 6b). Fig. 7 shows the bubble velocities along the flow direction. Here the red dot and the black dashed line denote the bubble velocity (u_b) and the tube-section average velocity (u_a), respectively. At the micro-gravity, the buoyancy force disappears, yielding the bubble velocity almost identical to the tube-section average velocity in the bare tube section, under which both phases have almost the same velocity and the slip ratio approaches one (see Fig. 7).

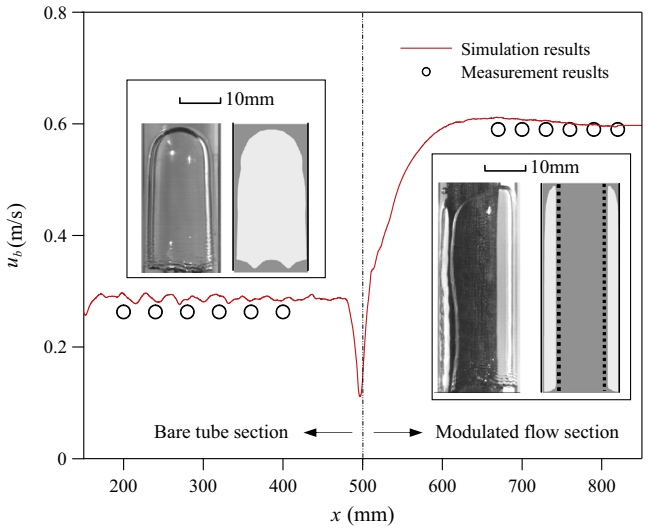

Fig. 5. Comparison of simulation results with measurement results at normal gravity.

Fig. 6c shows the bubble across the mesh cylinder region. When a bubble interacts with the mesh cylinder, it cannot breakthrough mesh pores due to the large surface energy required. Thus the bubble is enforced to flow in the annular region in the modulated flow section, forming the elongated-ring-slug-bubble to enclose the mesh cylinder. Due to the mesh pores "blocked" by the bubble interface, liquid at the mesh cylinder bottom is almost stationary. Chen et al. (2013) has performed the surface energy analysis in detail to explain why bubbles are difficult to breakthrough mesh pores and enter the core region. Usually, a large pressure difference is needed to penetrate a bubble interface within mesh pores. The smaller the mesh pores, the larger the pressure difference is, constructing the major mechanism for gas bubbles to flow in the annular region. Because of the bottom mesh pores blocked by the bubble interface leading to the decrease of the flowing area, the bubble across the mesh cylinder region accelerates to a peak velocity of 0.16 m/s (see Fig. 7).

In the modulated flow section, elongated-ring-slug bubbles are segmented in the annular region with gradually shortened liquid plugs (see Fig. 6d), until these segmented bubbles are completely merged (see Fig. 6e). Under the merged condition the whole annular region is full of gas except a very thin liquid film on the wall. The reason of bubble coalescence is that the bubble velocity decreases gradually along the flow direction in the annular region (see Fig. 7) due to the drag force induced by the tube wall and mesh cylinder surface, leading to liquids in liquid plugs flowing from the annular region to the core region. Fig. 8 shows the radial velocities (v) through mesh pores versus x and the near-pore-velocity fields. The negative sign represents the liquid from the annular region to the core region. Radial velocities through mesh pores reveal that the liquid plugs in the annular region always possess liquid flow from the annular region to the core region.

Case 2 and Case 3 have the same flow pattern modulation processes as Case 1, so the modulation processes for these two cases will not be repeated here.

Modulated flow parameters

Figs. 9–11 show the phase distributions in the bare tube section and modulated flow section for three different cases. The slug bubble length (L_g) is the length from a bubble front to the rear, and the

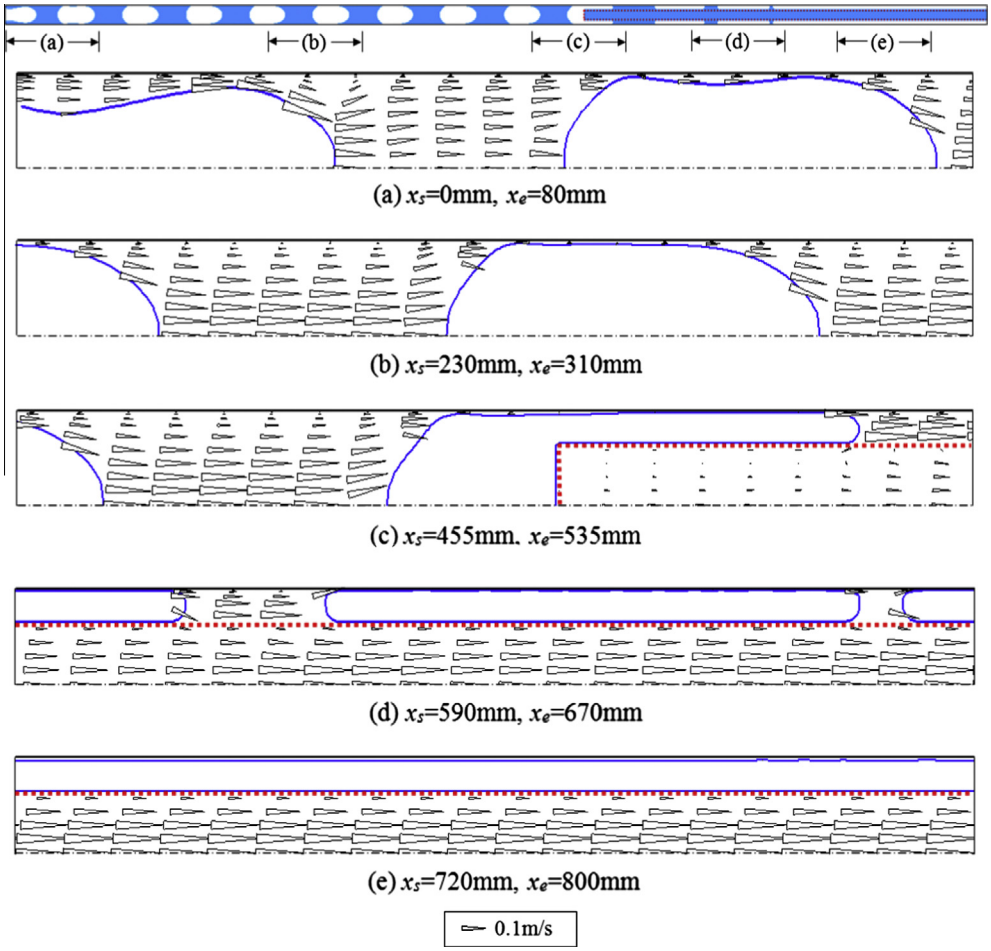

Fig. 6. Bubble shape and flow field in different sections for Case 1 when t = 7.933 s.

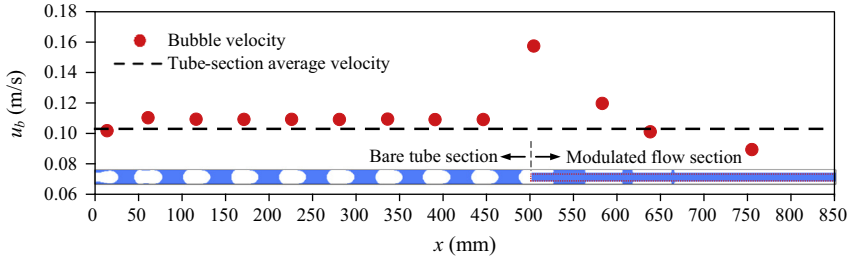

Fig. 7. Bubble velocities along the flow direction for Case 1 when t = 7.933 s.

liquid plug length (L_l) is the liquid length between two neighboring bubbles. We define the slug bubble length ratio in a unit of slug bubble and liquid plug as $\beta = L_g/(L_g + L_l)$. β denotes the bubble population density along the flow direction. In the bare tube section, the values of β are 0.56, 0.40 and 0.26 for Case 1, Case 2 and Case 3, respectively. It means that the value of β is reduced with the decrease of gas volume flow rate. The mesh screen surface significantly changes the phase distributions in the modulated flow section. The bubbles are enforced to flow in the annular region, following which they are completely merged with the whole annular region full of gas for three different cases. Thus values of β all equal to one. Table 3 gives the β values in both the bare tube section and modulated flow section for three cases.

Fig. 12 shows void fractions over the tube cross section for three cases. The time-averaged void fraction $\langle\alpha\rangle$ is defined as the integrated time with the grid cell occupied by the gas phase divided by the total time. In the bare tube section, $\langle\alpha\rangle$ are larger at the tube centerline ($r = 0$) and decreased away from the tube centerline for the three cases. Such phase distribution refers to "gas in the core and liquid on the wall", introducing a liquid thermal resistance for the condensation heat transfer. The inserted mesh cylinder creates an inverse phase distribution compared with those in the bare tube section. Void fractions are exact zero in the core region for the three cases, corresponding to the core region completely occupied by liquids. Void fractions equal to one in the annular region for the three cases, yielding a complete phase separation with "gas in the annular region and liquid in the core region", creating an ultra-thin liquid film on the wall.

Fig. 13 shows the liquid film thickness (δ), which is a key parameter to govern the condensation heat transfer. The solid

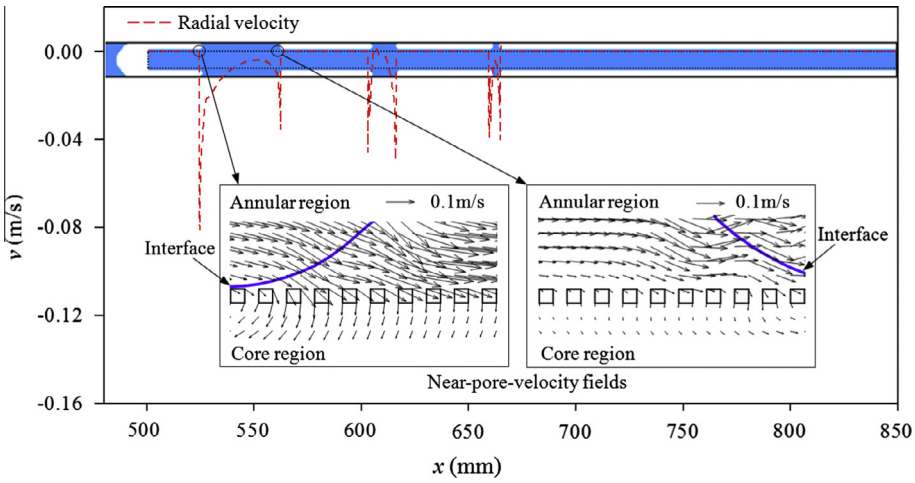

Fig. 8. Radial velocities through mesh pores and near-pore-field for Case 1 when t = 7.933 s.

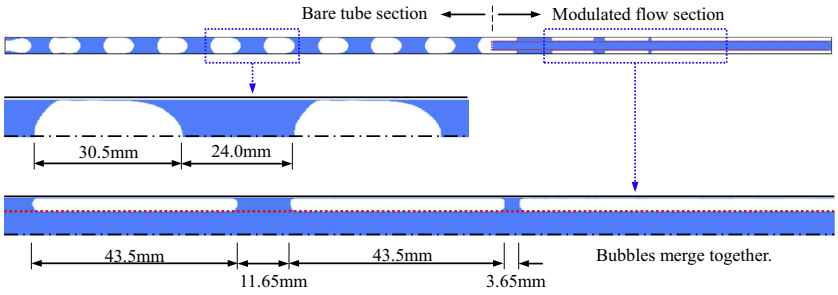

Fig. 9. The phase distribution in the bare tube section and modulated flow section for Case 1 when t = 7.933 s.

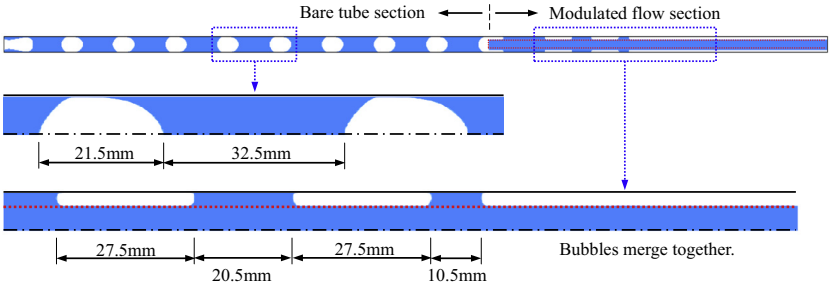

Fig. 10. The phase distribution in the bare tube section and modulated flow section for Case 2 when t = 12.29 s.

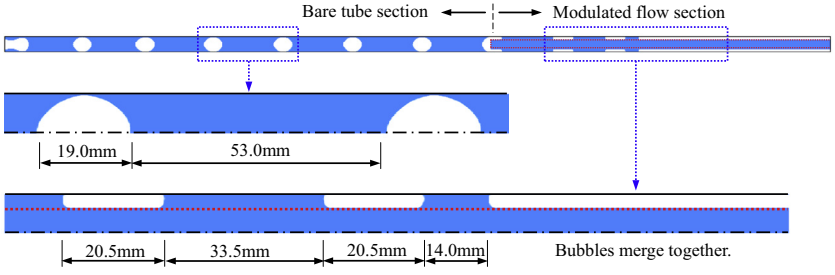

Fig. 11. The phase distribution in the bare tube section and modulated flow section for Case 3 when t = 18.08 s.

and dashed curves represent δ variations in the bare tube section and modulated flow section, respectively, while the black, blue and red curves refer to the values for Case 1, Case 2 and Case3, respectively. In order to make the results more clearly, we adopt a logarithm presentation for the vertical coordinate of δ. When the bubble is flowing in the bare tube section, δ are in the range of 0.12–7.85 mm for the three cases (see the solid curves of Fig. 13). When the bubbles are completed merged in the

Table 3
Flow parameters in both the bare tube section and modulated flow section for three different cases.

Case	Bare tube section			Modulated flow section			$\frac{(\beta/\delta_a)_m}{(\beta/\delta_a)_b}$
	β	δ_a (mm)	β/δ_a (1/mm)	β	δ_a (mm)	β/δ_a (1/mm)	
Case 1	0.56	0.397	1.411	1.00	0.049	20.41	14.46
Case 2	0.40	0.468	0.855	1.00	0.038	26.32	30.78
Case 3	0.26	0.959	0.271	1.00	0.035	28.57	105.42

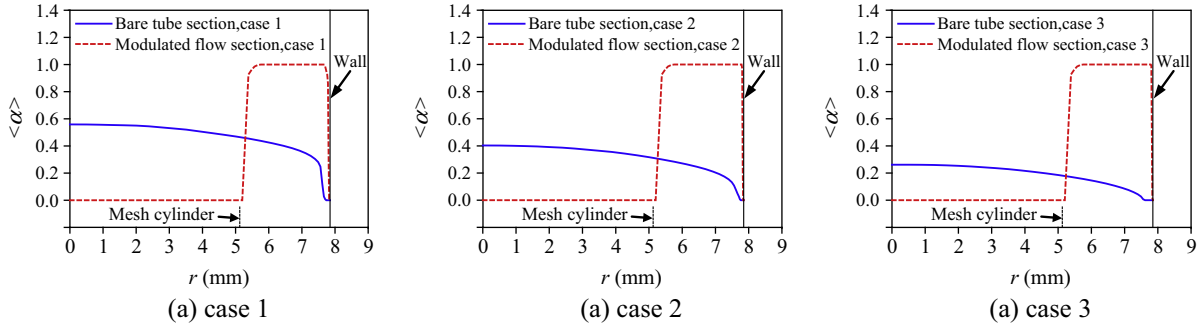

Fig. 12. Void fractions over the tube cross section for three different cases.

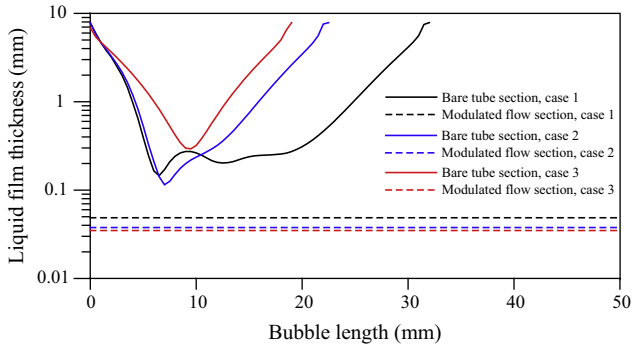

Fig. 13. Liquid film thicknesses in the bare tube section and modulated flow section for three different cases.

modulated flow section, δ are in the range of 35–49 μm for the three cases (see the dashed curves of Fig. 13). δ for the merged bubbles in the modulated flow section are significantly decreased compared to those in the bare tube section.

Because δ are varied along the bubble length in the bare tube section, an averaged liquid film thickness (δ_a) is defined as follows

$$\delta_a = L_g \Big/ \int_0^{L_g} \frac{1}{\delta} dx \tag{14}$$

In the modulated flow section, δ remain almost constant along the flow direction under the merged condition, so δ_a can be defined that $\delta_a = \delta$.

Table 3 gives the averaged liquid film thicknesses in both the bare tube section and modulated flow section for the three cases. It can be concluded that: (a) the liquid film thicknesses are increased with the decrease of gas volume flow rate in the bare tube section from Case 1 to Case 3; (b) the liquid film thicknesses are reduced with the decrease of gas volume flow rate in the modulated flow section; (c) the liquid film thickness in the modulated flow section is decreased to 12.3% of that in the bare tube section for Case 1; the liquid film thickness is decreased to 8.1% for Case 2; the liquid film thickness is decreased to 3.6% for Case 3.

Condensation rate prediction related to modulated bubble dynamics

Based on the modulated bubble dynamics and parameters by the inserted mesh cylinder, we estimate the condensation heat transfer enhancement by the flow pattern modulation technique. The condensation rate for a slug bubble is defined as

$$\dot{M} = \frac{Q}{h_{lg}} = \frac{\int_0^{L_g} \pi D \lambda_l \frac{T_{sat}-T_w}{\delta} dx}{h_{lg}} = \frac{\pi D L_g \lambda_l (T_{sat}-T_w)}{h_{lg}\delta_a} \tag{15}$$

where λ_l is the liquid thermal conductivity, h_{lg} is the latent heat, T_w is the wall temperature and T_{sat} is the saturation temperature.

Then the condensation rate per unit wall area can be written as

$$\dot{m} = \frac{\dot{M}}{\pi D(L_g+L_l)} = \frac{\lambda_l(T_w-T_{sat})}{h_{lg}} \times \frac{L_g}{L_g+L_l} \times \frac{1}{\delta_a} = \frac{\lambda_l(T_w-T_{sat})}{h_{lg}} \times \frac{\beta}{\delta_a} \tag{16}$$

In Eq. (16) λ_l, h_{lg}, T_w and T_{sat} are all considered as constant. Then $\dot{m}$ is direct proportion to a combined parameter of $\beta\delta_a$. This parameter synthesizes the effect of bubble population density (β) and averaged liquid film thickness (δ_a). Table 3 shows $\beta\delta_a$ in both the bare tube section and modulated flow section. $\beta\delta_a$ in the modulated flow section are 14.46, 30.78, 105.42 times of those in the bare tube section for Case 1, Case 2 and Case 3, respectively, indicating that $\dot{m}$ is significantly enhanced by the flow pattern modulation for slug flows and the ratio of $\dot{m}_m/\dot{m}_b$is increased with the decrease of gas volume flow rate.

Conclusion

In this paper, we analyze the flow pattern modulation process and predict the condensation rate in the phase separation condenser tube at micro-gravity environment for three different slug flows. The following conclusions can be drawn:

- The inserted mesh cylinder modulates the slug flow in the bare tube section to form the elongated-ring-slug bubble train in the modulated flow section. Liquid plugs can disappear due to the continuous liquid flow from the annular region to the core

region. Thus the two-phases are thoroughly separated with gas flowing in the annular region, forming ultra-thin liquid film thicknesses on the wall under micro-gravity environment.

- In the bare tube section, the bubble population density (β) is reduced with the decrease of gas volume flow rate. In the modulated flow section, the whole annular region is full of gas, meaning that the β values are all equal to one.
- The modulated liquid film thicknesses are decreased to about 1/30–1/10 of those in the bare tube section for the three cases.
- The condensation rates per unit wall area ($\dot{m}$) is significantly enhanced by the flow pattern modulation technique. $\dot{m}$ in the modulated flow section are about 10–100 times of those in the bare tube section for the three cases and the ratio of $\dot{m}_m/\dot{m}_b$ is increased with the decrease of gas volume flow rate.
- This study proves the effectiveness of the phase separation condenser tube at micro-gravity environment.

Acknowledgements

This work was supported by the Natural Science Foundation of China (51476054), the Natural Science Foundation of China of International Cooperation Project (Grant No. 51210011) and the Program for New Century Excellent Talents in University of China (NCET-13-0792).

References

Brackbill, J.U., Kothe, D.B., Zemach, C., 1992. A continuum method for modeling surface tension. J. Comput. Phys. 100, 335–354.
Cavallini, A., Del Col, D., Doretti, L., Longo, G.A., Rossetto, L., 2000. Heat transfer and pressure drop during condensation of refrigerants inside horizontal enhanced. Int. J. Refrig. 23, 4–25.
Chen, H.X., Xu, J.L., Li, Z.J., Xing, F., Xie, J., Wang, W., Zhang, W., 2012. Flow pattern modulation in a horizontal tube by the passive phase separation concept. Int. J. Multiph. Flow 45, 12–23.
Chen, Q.C., Xu, J.L., Sun, D.L., Cao, Z., Xie, J., Xing, F., 2013. Numerical simulation of the modulated flow pattern for vertical upflows by the phase separation concept. Int. J. Multiph. Flow 56, 105–118.
Da Riva, I., Sanz, A., 1991. Condensation in ducts. Microgravity Sci. Technol. 4, 179–187.
Delil, A.A.M., 1998. On thermal-Gravitational Modeling, Scaling and Flow Pattern Mapping Issues of Two-Phase Heat Transport Systems. National Aerospace Laboratory, Albuquerque, USA.
Delil, A.A.M., Woering, A.A., Verlaat, B., 2002. Development of a Mechanically Pumped Two-Phase CO_2 Cooling Loop for the AMS-02 Tracker Experiment. Conference of Technology & Applications International Forum. National Aerospace Laboratory, Albuquerque, USA.
Graham, D., Chato, J.C., Newell, T.A., 1998. Heat transfer and pressure drop during condensation of refrigerant 134a in an axially grooved tube. Int. J. Heat Mass Transf. 42, 1935–1944.
Haobo, J., Reinhard, R., 2002. A distributed model of a space heat pump under transient conditions. Int. J. Energy Res. 27, 145–160.
Hirt, C.W., Nichols, B.D., 1981. Volume of fluid (VOF) method for the dynamics of free boundary. J. Comput. Phys. 39, 201–225.
Kaya, T., Pérez, R., Gregori, C., Torres, A., 2008. Numerical simulation of transient operation of loop heat pipes. Appl. Therm. Eng. 28, 967–974.
Kim, S.M., Mudawar, I., 2012. Theoretical model for annular flow condensation in rectangular micro-channels. Int. J. Heat Mass Transf. 55, 958–970.
Mehdizadeh, A., Sherif, S.A., Lear, W.E., 2011. Numerical simulation of thermofluid characteristics of two-phase flow in microchannels. Int. J. Heat Mass Transf. 54, 3457–3465.
Miyara, A., Otsubo, Y., 2002. Condensation heat transfer of herringbone micro fin tubes. Int. J. Therm. Sci. 41, 639–645.
Morales-Ruiz, S., Rigola, J., Rodriguez, I., Oliva, A., 2012. Numerical resolution of the liquid-vapour two-phase flow by means of the two-fluid model and a pressure based method. Int. J. Multiph. Flow 43, 118–130.
Patankar, S.V., 1980. Numerical Heat Transfer and Fluid Flow. Hemisphere, Washington, DC.
Salewski, M., Fuchs, L., 2007. Consistency issues of Lagrangian particle tracking applied to a spray jet in crossflow. Int. J. Multiph. Flow 33, 394–410.
Sun, D.L., Xu, J.L., Chen, Q.C., Cao, Z., 2013. Numerical study of flow pattern modulation in a vertical phase separation condenser tube. Chin. Sci. Bull. 58, 1592–1598.
Suriyan, L., Somchai, W., 2010. The effects of corrugation pitch on the condensation heat transfer coefficient and pressure drop of R134a inside horizontal corrugated tube. Int. J. Heat Mass Transf. 53, 2924–2931.
Tao, W.Q., 2001. Numerical Heat Transfer, second ed. Xi'an Jiaotong University Press, Xi'an, China.
Zu, Y.Q., Yan, Y.Y., 2009. A numerical investigation of electrohydrodynamic (EHD) effects on bubble deformation under pseudo-nucleate boiling conditions. Int. J. Heat Fluid Flow 30 (4), 761–767.
Zu, Y.Q., Yan, Y.Y., Gedupudi, S., Karayiannis, T.G., Kenning, D.B.R., 2011. Confined bubble growth during flow boiling in a mini/micro-channel of rectangular cross-section Part II: approximate 3-D numerical simulation. Int. J. Therm. Sci. 50 (3), 267–273.